Site occupancies in a chemically complex σ-phase from the high-entropy Cr–Mn–Fe–Co–Ni system

Jean-Marc Joubert, Yordan Kalchev, Andrea Fantin, Jean-Claude Crivello, Rico Zehl, Erik Elkaïm, Guillaume Laplanche

Site occupancies in a chemically complex σ-phase from the high-entropy Cr–Mn–Fe–Co–Ni system

Jean-Marc Joubert[1], Yordan Kalchev[2], Andrea Fantin[3,4], Jean-Claude Crivello[1], Rico Zehl[2], Erik Elkaïm[5], Guillaume Laplanche[2]

[1] Univ Paris Est Creteil, CNRS, ICMPE, UMR 7182, 2 rue Henri Dunant, 94320 Thiais, France

[2] Ruhr-Universität Bochum, Institute for Materials, Universitätsstrasse 150, 44780 Bochum, Germany

[3] Technische Universität Berlin, Hardenbergstr. 36, 10623 Berlin, Germany

[4] Helmholtz-Zentrum Berlin für Materialien und Energie, Hahn-Meitner-Platz 1, 14109 Berlin, Germany

[5] Synchrotron SOLEIL, L'Orme des Merisiers, 91192 Gif-sur-Yvette, France

Abstract

Site occupancies in a single-phase σ-intermetallic compound of composition $Cr_{46}Mn_{15.2}Fe_{16.3}Co_{17}Ni_{5.5}$ (in at.%) were studied. To the best of the authors' knowledge, such a complex analysis with 5 elements occupying 5 different sites has never been tackled before and is addressed here using cutting edge X-ray diffraction techniques, absorption spectroscopy and simulations. Resonant powder diffraction data were collected at the K-edges of each of the five elements and the site occupancies were refined by a joint Rietveld analysis. Dispersion coefficients were retrieved independently from tabulated values, Kramers-Kronig relations and reference samples. Additional Extended X-ray Absorption Fine Structure (EXAFS) measurements were used to confirm the site occupancies and bond lengths. The site occupancies were independently obtained by a thermodynamic approach based on the enthalpies of formation of the $5^5 = 3125$ configurations generated by the ordered distribution of the five components on the five sublattices, derived from a machine learning approach based on a DFT database. Overall, the calculations and experiments are in excellent agreement and reveal that the σ phase can accommodate a considerable degree of disorder, which consequences for thermodynamic modelling are discussed. The configurational entropy (S) of the σ phase represents 84% of that of a fully disordered alloy with the same composition, which is much larger than that expected for a fully ordered intermetallic phase ($S = 0$). The corresponding entropic stabilization is one of the reasons for the fact that the σ phase is one of the most important intermetallic that precipitates in high-entropy alloys and many engineering materials.

keywords: CoCrFeMnNi; resonant diffraction; anomalous diffraction; machine learning; site occupancies; sigma phase; high-entropy alloys; EXAFS; XANES; TCP phases

1. Introduction

One of the best-known and most widely studied topologically close-packed (TCP) phases is probably the σ phase [1, 2] that forms in several engineering alloys such as austenitic stainless steels [3], Ni-base superalloys [4], and high-entropy alloys (HEAs) [5] when these materials are subjected to high temperatures for long times [6]. It is the one of the most commonly reported intermetallic compound for two reasons: it appears in a very large number of binary systems comprising transition metals (43 systems [1]), and it is at least partially stabilized by configurational entropy in compositionally complex alloys, a feature that is addressed in the present work. The precipitation of the σ phase in engineering alloys is detrimental as it embrittles them [7, 8] and reduces their corrosion resistance [9]. It is therefore of prime importance to predict how certain elements stabilize this phase and affect its precipitation kinetics [6, 10, 11] and to characterize the intrinsic properties of the σ phase in terms of elastic properties, strength, toughness, diffusivities, etc. To date, such information is still lacking for compositionally complex alloys.

Recently, Kishida *et al.* [12] investigated the mechanical properties of the binary and equiatomic CrFe σ phase by micropillar compression and micro-cantilever bend tests at room temperature (RT). The critical resolved shear stresses (CRSS) for the glide of zonal dislocations were found to be very large (> 1.3 GPa) while the fracture toughness remained very low (1.6-1.8 $MPa \cdot m^{1/2}$). Therefore, the stress required to initiate crack growth is significantly lower than the CRSS for dislocation slip in large specimens (> 1 mm), leading to an extremely brittle behavior. As the σ phase is extremely hard and brittle, conventional mm-sized specimens cannot be machined, precluding the use of most experimental test methods. In this context, density functional theory (DFT) calculations can be performed to assess several properties of this phase, but their quality and correctness rely on the crystallographic description of this phase, i.e., how certain elements partition to different sublattices, which is addressed here for the $Cr_{46.0}Mn_{15.2}Fe_{16.3}Co_{17.0}Ni_{5.5}$ (at.%) σ phase [6]. This composition is found in equilibrium with an *fcc* phase in a HEA of composition $Cr_{26}Mn_{20}Fe_{20}Co_{20}Ni_{14}$ derived from the Cantor alloy ($Cr_{20}Mn_{20}Fe_{20}Co_{20}Ni_{20}$) [13].

The σ phase crystallizes in space group $P4_2/mnm$ (CrFe structure type) with 30 atoms per unit cell among five different Wyckoff sites (2*a*, 4*f*, 8i_1, 8i_2, 8*j*) with different coordination numbers (CN12, 15, 14, 12, 14, respectively) on which an unusually strong occupational disorder occurs [1], i.e., all the sites may be occupied by different elements with different site occupancies. For a detailed description of the crystal structure, the reader is referred to Ref. [1]. The crystal structure and the coordination polyhedra around each site are displayed in Fig. 1. The detailed site environment is shown in Table S1.

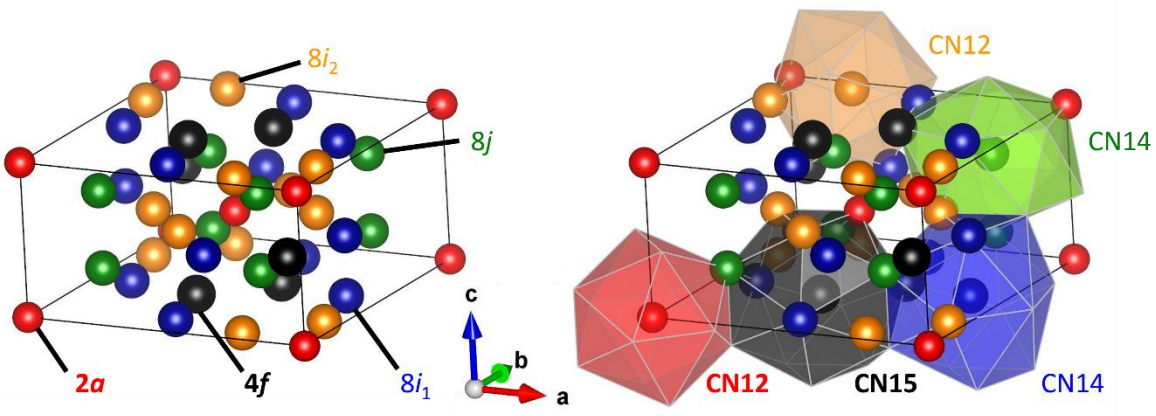

Fig. 1. Crystal structure of the σ phase showing the different Wyckoff positions (left) and the coordination polyhedra around each site.

The objective of the present study is to establish the site occupancies in a quinary and chemically complex σ phase with composition $Cr_{46}Mn_{15.2}Fe_{16.3}Co_{17}Ni_{5.5}$. Due to the large extent of occupational disorder in this structure, the five non-equivalent sites may be occupied (differently) by all five elements. Such a complex problem has, to the best of the authors' knowledge, never been resolved in the literature and it can only be addressed experimentally using resonant powder diffraction measured at the K-edges of the five elements. The element specific X-ray Absorption Near-Edge Structure (XANES) and Extended X-ray Absorption Fine structure (EXAFS) techniques were also employed to answer specific points useful to consolidate the resonant powder diffraction measurements, analyses and results. XANES, performed at the K-edge of each σ-phase alloying element Cr, Mn, Fe, Co and Ni, together with the corresponding reference pure metals, allowed the calibration of the energy scale, crucial for the successful diffraction data collection and subsequent refinements. EXAFS, on the other hand, allowed to determine accurately the local bond lengths around each element, inferring qualitative and quantitative information on site occupancy and atomic positions in the crystal structure. Finally, the experimental EXAFS spectra allowed the calculation of dispersion coefficients *f'* , independently of tabulated values, through the Kramers-Kronig relation (KKR), an ulterior approach to carry out structural refinements and exhaustively validate the results of resonant powder diffraction measurements.

Site occupancies may be also calculated using a thermodynamic model based on the Bragg-Williams approximation [14]. The Gibbs energy of the σ phase has an enthalpic and an entropic term. The enthalpy is approximated by a rule of mixing related to the amount of each component in each sublattice without considering interactions on the sublattices, while the entropy contribution is calculated considering only the configurational entropy. At each temperature, the atomic distribution minimizing the energy can be found from the knowledge of the energy of every ordered configuration generated by the system. In the present work, $5^5 = 3125$ configurations have been generated by the distribution of 5 elements on 5 sublattices. The energy of each configuration has been obtained by a machine learning approach based on a learning database constating of a subset of DFT calculations [15]. The comparison between experiments and calculations will be shown.

2. Background for the resonant X-ray diffraction measurement

The determination of site occupancies by diffraction is limited by two constraints. (*i*) The diffraction contrast between different atoms present on the same site(s) should be sufficient so that they can be distinguished: in the case of X-ray diffraction (XRD), their number of electrons (or atomic number) should be sufficiently different. (*ii*) Only one occupancy parameter per site can be obtained from a diffraction dataset. Basically, this is because diffraction 'sees' only an average of the scattering density at each site. In summary, provided that the atomic numbers of two atoms *A* and *B*, sharing the same site(s), are sufficiently different, that there is no vacancy on the site(s), and that the alloy composition is known, site occupancies of *A* and *B* can be determined on all the sites of the structure. Technically, diffraction is therefore limited by the number of atoms but not by the number of sites. In this study, with the five elements Cr, Mn, Fe, Co and Ni, one faces two problems simultaneously. First, the contrast between elements is insufficient, as they are neighbors in the periodic table. Second, if all the elements share the same sites, at least four diffraction patterns, each with sufficient contrast between elements, are required to unambiguously determine all site occupancies. This issue can be tackled only with resonant XRD since this is the only technique allowing to enhance the contrast between selected elements close to each other in the periodic table by collecting different datasets at specific energies. It is based on the observation that, close to the absorption edge of an element (K-edges in the present case), the scattering power of the atom f_0 (normally proportional to the atomic number) is strongly reduced by a quantity f' depending on the energy of the incident beam following:

$$f = f_0 + f' + i\,f'' \qquad (1)$$

where f' (negative) and f'' are the real (dispersive) and imaginary (absorptive) components of the resonant scattering coefficient. By recording diffraction patterns measured with an X-ray energy close to each of the edges of the different elements, one obtains sufficient data to solve the complete problem. For a review and some examples, the reader may refer to Refs. [16-19]. In principle, the resonant XRD technique is not limited by the number of elements it can analyze but, to the best of the authors' knowledge, no other report about such a complex system consisting of five elements and five sites has been reported in literature so far.

What also makes this experiment tedious is the very high absorption of the sample at almost all the edges. The calculated linear absorption coefficient (μ) is shown in Fig. 2. For most edges, it reaches nearly 2000 cm^{-1}, representing a typical penetration depth of only 5 µm, approximately the average size of a single particle of the powder. For this reason, as fine particles as possible were sieved. In addition, the powder of the quinary σ phase was diluted with a glass powder to reduce sample absorption. Note that, even for extremely brittle intermetallic systems, such as the present σ phase, it is very complex to attain small particle sizes because of possible cold work deformation.

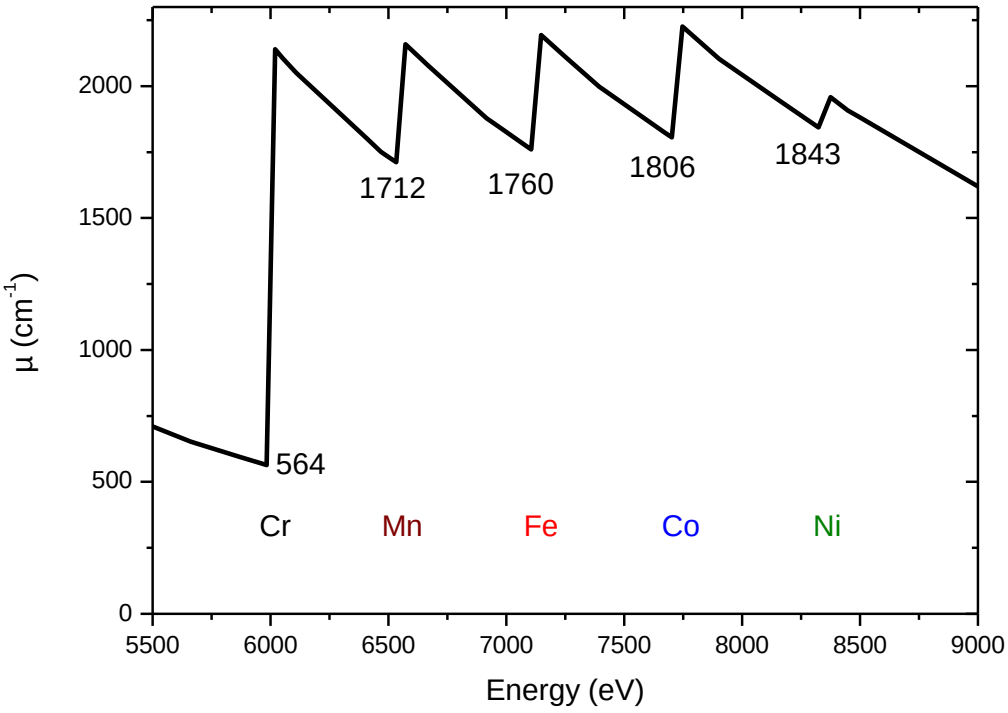

Fig. 2. Calculated linear absorption of the $Cr_{46.0}Mn_{15.2}Fe_{16.3}Co_{17.0}Ni_{5.5}$ (at.%) σ phase as a function of the X-ray energy. The absorption values μ before each different K-edge, corresponding to the energy at which diffraction patterns were recorded, are also depicted.

In Eq. 1, the *f'* values can be obtained from Sasaki's tables [20], for which the Cromer and Liberman method was used [21, 22], provided that the energy is not chosen too close to the edges (above 5 eV). The energy position of the edge should be, of course, clearly defined in the sample itself. Advantageously, as in intermetallic compounds atoms carry negligible charges, the edge position (relative to the pure metal) is not affected and the dispersion curve (*f'* function of energy) is very similar to that of the free atom. Alternatively, *f'* values can be calculated by recording the X-ray absorption coefficient as a function of the energy (i.e., the absorptive component *f''* in Eq. 1) and using KKR [23]. Both approaches were compared in the present work. Additionally, standards, with known site occupancies from neutron diffraction, have been used to obtain the *f'* values by a third manner.

3. Experimental details

3.1. Materials

A button weighing 70 g with a nominal composition of $Cr_{46.0}Mn_{15.2}Fe_{16.3}Co_{17.0}Ni_{5.5}$ (in at. %) was arc melted under a protective Ar atmosphere, starting with pure metals (purity ≥ 99.89 wt.%). The button was flipped and remelted four times to ensure a homogeneous chemical composition and

slowly cooled. Finally, the button was encapsulated in a fused silica tube and homogenized at 1100°C for 72 hours and furnace cooled to minimize thermal stress and prevent crack formation. Further details can be found in Ref. [10].

The reference sample $Mn_{60}Co_{40}$ used for Mn and Co edges was synthesized by sintering pure elemental powders at 900°C for 14 days in a fused silica tube. Its composition was characterized with a microprobe while its single-phase character was checked by XRD. The site occupancies were determined using neutron diffraction. The details of the preparation and characterization of this sample may be found in Ref. [24]. Note that neutron diffraction refined occupancy values are accurate and can be used because of the substantially different (of opposite sign) neutron coherent scattering lengths of Mn and Co (b_{Mn} = -3.73 fm, b_{Co} = + 2.49 fm). A second standard sample (MnNi for Ni edge) was also synthesized but did not prove to be useful. This is probably due to the lack of contrast between Ni in resonant conditions and Mn ($Z_{Mn} = Z_{Ni}$-3).

3.2. Sample preparation

In order to prepare the samples for the synchrotron experiments, the σ powder was sieved to obtain particles with sizes smaller than 10 µm. Backscatter electron (BSE) micrographs were recorded, binarized using the ImageJ software (see Fig. S1), and hence the average particle size was measured. A second run through the 10 µm sieve was conducted. The first particles going through the sieve were selected which guaranteed that only the finest particles were finally adopted in the experiment. The same process was used to prepare a fine powder from the binary reference $Mn_{60}Co_{40}$. Glass capillaries with a diameter of 0.3 mm were filled with undiluted powder, using a Huber vibratory machine and an ultrasonic bath to obtain a homogeneous distribution of the particles. Then, a glass powder was obtained from a batch of glass capillaries, processed in a mortar, and sieved with a 10 µm opening-sized sieve. It was used to dilute the sample powder to 50 wt.% or 25 wt.%. Both the quinary σ phase and the standard $Mn_{60}Co_{40}$ powders were processed that way and at least two powder-filled glass capillaries, with a diameter of 0.2 mm, were prepared and sealed for each alloy. Such a preparation is the best compromise between a reasonable absorption and a decent scattering signal for any X-ray energy chosen in the resonant diffraction experiment.

3.3. Resonant XRD experiments and XANES measurements at SOLEIL

Powder diffraction measurements were performed on the CRISTAL beamline at SOLEIL synchrotron source at high energy (18469 eV) and selected energies below Cr (5989 eV), Mn (6539 eV), Fe (7112 eV), Co (7709 eV) and Ni (8333 eV) K-edges. Diagrams were collected in Debye-Scherrer geometry, with rotating capillaries, using a detection system made of 9 linear Mythen modules covering a 50° 2θ circle arc at 720 mm from the sample, allowing for high-quality patterns for all samples at all energies. NIST silicon 640b reference powder was measured at all energies to refine the wavelength. The energy was selected using a Si (111) monochromator. Prior to diffraction measurements, XANES spectra were systematically acquired in fluorescence mode (1 eV resolution)

on reference pure metal foils (5 to 7 µm thickness), using an SDD Rontec detector, to ascertain the exact energy position of the different edges for calibration purposes. The absorption edge energy, E_0, is defined as the energy corresponding to the first inflection point of the absorption spectrum. Normalization and self-absorption correction were performed using the software ATHENA [25]. Finally, measurements in resonant conditions were systematically carried out at 7 eV below each edge.

3.4. XANES and EXAFS measurements at ESRF

XANES and EXAFS spectra were obtained for each K-edge of the σ phase at the LISA (BM-08) beamline at the ESRF on specimens prepared from the same sieved powder used in the resonant diffraction experiment. Samples were measured using a pair of Si (311) flat monochromator crystals. Higher harmonics rejection was obtained through Si-coated collimating/focusing mirrors (E_{cutoff} = 15 keV). Data on specimens and pure metal foil references were measured in transmission mode. Specimens were measured at RT, in the XANES region with a fixed energy step of 1.5 eV, and in the EXAFS region with a fixed *k* step of 0.05 $Å^{-1}$ up to a maximum value of about 12 $Å^{-1}$. Intrinsic range limitations were present for all elements but Ni K-edge, given the presence of the neighboring *Z*+1 element (*Z*: atomic number) in the alloy. For Ni K-edge, data up to 15 $Å^{-1}$ was acquired. Reference foils were measured up to k_{max} = 18 $Å^{-1}$. Details on XANES/EXAFS data treatment and measurement details are reported in Supplementary Materials.

KKR calculations were then carried out according to the routines described in Ref. [26] to determine *f'* using the experimentally determined σ phase chemical composition. The *f'* functions were calculated from a KKR transform of *f''*. The latter functions were obtained from the experimental data measured at each edge with LISA. The corresponding µ(E) functions were adapted (via multiplicative scaling plus a linear background) to follow the *f''* of the Windt tables to match the *f''* in value and first derivative before and after the edge. This resulted in *f''* functions with a wide energy range and accurate shape around the edge, suitable for the KKR transform.

Refinements of EXAFS data were conducted assuming a binary model (details can be found elsewhere [27]), because of the impossibility to discriminate any of the alloying elements from the others. Therefore, for the first shell and each Wyckoff site, only paths given by Absorber-grey metal (*Abs-M*) were employed. The grey metal *M* used as alloy approximation was Mn, the closest element to the weighted average of *Z* numbers according to stoichiometry, having therefore *Abs-M* paths with *Abs*: Cr, Mn, Fe, Co and Ni. The amplitude parameters S_0^2 for each absorber were fixed to those obtained from refining the corresponding reference foil, while disorder (σ^2, related to the Debye-Waller factor) was modeled on a Debye function and refined with a single parameter, namely the Debye temperature.

3.5. Rietveld refinement

The diffraction data have been analyzed using the Rietveld method with the Fullprof program [28, 29]. The minor secondary phases (less than 1 Vol.%) detected in each sample have been

considered. The dispersion coefficients *f'* and *f''* in Eq. 1 were obtained from Sasaki's tables [20]. It was not possible to obtain *f'* from the XANES signal recorded on the CRISTAL beamline at SOLEIL using the KKR because the energy range that could be accessed was too limited. For instance, towards lower energy, further measurements would have needed a change of the undulator harmonic. This is the reason why measurements were not performed too close to the edge and why standards were used, so that the calculated theoretical values could be safely used. However, *f'* values could be successfully determined from the EXAFS measurements carried out at the ESRF. The complete list of *f'* and *f''* values is given as a spreadsheet file provided in Supplementary Materials. Refinements were conducted using both Sasaki and KKR values. From Sasaki, the *f'* values obtained for the elements in resonant conditions range between -6.74 e^- and -6.96 e^-.

It is impossible to separate the contributions of sample absorption and of atomic displacement parameters to the diffraction. Absorption cannot be obtained satisfactorily since the amount of σ phase in the capillaries cannot be determined. An arbitrary absorption correction was included, and an overall *B* displacement parameter was refined knowing that the obtained value is not meaningful. This has no consequence for the refinement of the other parameters since the approximate absorption correction is compensated by the *B* parameter which is not important in the present study.

The background of the XRD patterns was interpolated between carefully chosen points. Atomic coordinates were refined using the pattern obtained at 18 keV and fixed to these values for the low-energy patterns. The diffraction peaks have a super-Lorentzian shape. This is typical for intermetallic compounds and corresponds to the presence in the sample of different states of strains related to cold work. They could be described, based on the presence of two distinct strain states, by two 'phases' in the Rietveld program with different line widths (broad corresponding to a cold-worked and narrow corresponding to a non-deformed state), all the other parameters being equal and constrained between the two 'phases'.

The site occupancies were constrained such as to reproduce the known composition of the σ phase and the full occupancy of each site (no vacancy). For 5 elements and 5 sites, this leaves 16 free parameters (4 parameters – the other one being constrained by the full occupancy – for each of the 4 first sites – the occupancies on the 5^{th} site being constrained by the overall composition). The way to constrain the occupancy parameters was detailed in Ref. [30] and was already used in many of the authors' previous studies [2, 31-33]. It consists in adding fictive atoms for each correlation that needs to be made. In the present case, 64 atom lines are required for the Fullprof input file. The obtained standard deviation is that given by the refinement program. It is based on a purely statistical analysis and neglects the effects of systematic errors in the model that are difficult to estimate. The Fullprof manual suggests that a better estimate of the real accuracy could be obtained by multiplying the standard deviation by ~3 (according to Bérar and Lelann's formula [34].

4. Calculation details

The site occupancies of the σ phase in which substitutional disorder exists can be calculated at a finite temperature *T* by minimizing its Gibbs energy, G^{σ}, as conducted in the framework of the Calphad approach. The σ phase is treated with the Compound Energy Formalism [35] in the Bragg-Williams-Gorsky approximation, i.e., considering only the configurational entropy ^{conf}S and neglecting the entropy from atomic correlations and excess interaction parameters within the same sublattice [14]:

$$G^{\sigma} = {}^{srf}G - T \cdot {}^{conf}S \qquad (2)$$

where the surface of reference energy is described by:

$${}^{srf}G = \sum_{ijklm}^{\{Co,Cr,Fe,Mn,Ni\}} \left(y_i^{(2a)} y_j^{(4f)} y_k^{(8i1)} y_l^{(8i2)} y_m^{(8j)} \right) \Delta^{for} H(ijklm) \qquad (3)$$

The *ijklm* variables designate elements among {Co, Cr, Fe, Mn, Ni} distributed in the 5 sites *s* {2*a*, 4*f*, 8i_1, 8i_2, 8*j*}. For each *s* site of Wyckoff multiplicity a^s, the sum of atomic site fractions y^s is normalized as $\sum_k y_k^s = 1$, and the configurational entropy ^{conf}S is given by:

$${}^{conf}S = -R \sum_s a^s \sum_i y^s \ln y^s \qquad (4)$$

To be minimized by an external tool like Thermo-Calc, ^{srf}G requires the definition of every $\Delta^{for} H(ijklm)$ terms, i.e., the heat of formation of every $5^5 = 3125$ *ijklm* ordered configurations. First principles calculations in the frame of the DFT method have been used to estimate a part of all $\Delta^{for} H(ijklm)$ by the total energy difference with pure elements in their stable reference state.

The DFT calculations have all been carried out in conditions similar to those detailed in a previous work [36]. As implemented in the Vienna *Ab initio* Simulation Package (VASP), the Projector Augmented Wave (PAW) pseudo-potentials method was used [37, 38]. Exchange and correlations were considered in the Generalized Gradient Approximation (GGA) with the Perdew-Burke-Ernzerhof (PBE) functional [39, 40] with a 400 eV cutoff energy and 8×8×15 k-meshing samplings generated by the Monkhorst-Pack procedure [41]. Both the lattice parameters and atomic coordinates were fully relaxed through several intermediate steps. Magnetism was not considered since routine calculations with spin polarization are not robust enough for a correct energy prediction and because the relative ground state configurations are known to remain almost unchanged [42].

Initially, only 1295 among the 3125 possible configurations were calculated by DFT, including all the configurations in the Cr–Fe–Mn–Ni quaternary system, all the configurations in the Co–Fe–Ni ternary system, and all the configurations in all the binary (10) systems. The other configurations were then predicted using a regressor machine learning process using Multi-layer Perceptron from the Scikit-learn package [43]. The supervised training database was built using about 10,000 consistent DFT calculations on the σ phase generated from 14 different elements and by using additional physical descriptors such as atomic radii. All the details of the learning process and neural network optimization are given in a previous paper [15]. From an independent testing set, a root mean squared error of 3.6 kJ/mol on $\Delta^{for} H(ijklm)$ was estimated on the whole composition range. Then, the five-dimension convex hull was analyzed showing additional configurations (not initially calculated) that were close to the stability: 4 quaternary and about 20 ternary configurations containing Co. These new

configurations were finally calculated by DFT to reinforce the ground state description and to increase the accuracy of the prediction.

With the five-component database constructed, Thermo-Calc (2022) was used to compute site occupancies at 1000 K, a temperature compatible with the specimen preparation conditions.

5. Results

5.1. Characterization of the samples

The microstructural characterization of the quinary σ phase after homogenization is presented in the Supplementary Materials (see Fig. S2). In short, the quinary alloy is mostly single phase (>99 Vol.% σ phase) with a coarse-grained microstructure and exhibits large cracks. The minor phases were identified as a Cr-rich oxide (spinel) and a disordered *fcc* solid solution in Ref. [10]. Their presence was further confirmed by XRD and these minor phases were considered in the Rietveld refinement of the resonant XRD data.

5.2. XANES and EXAFS measurements

Energy calibration prior to each resonant diffraction measurement was carried out at SOLEIL by superimposing reference metal foils and σ K-edge XANES spectra, depicted in Fig. 3, establishing the relative energy position of σ K-edges to the known metallic foil ones. Edge energy positions correspond to the first inflection points in each spectrum, determined at the maximum of the first derivatives. At any edge, the difference between the edge energy of the references and corresponding K-edges in σ remains below 1 eV (cf. Table S2), in other words below the energy resolution of the CRISTAL beamline.

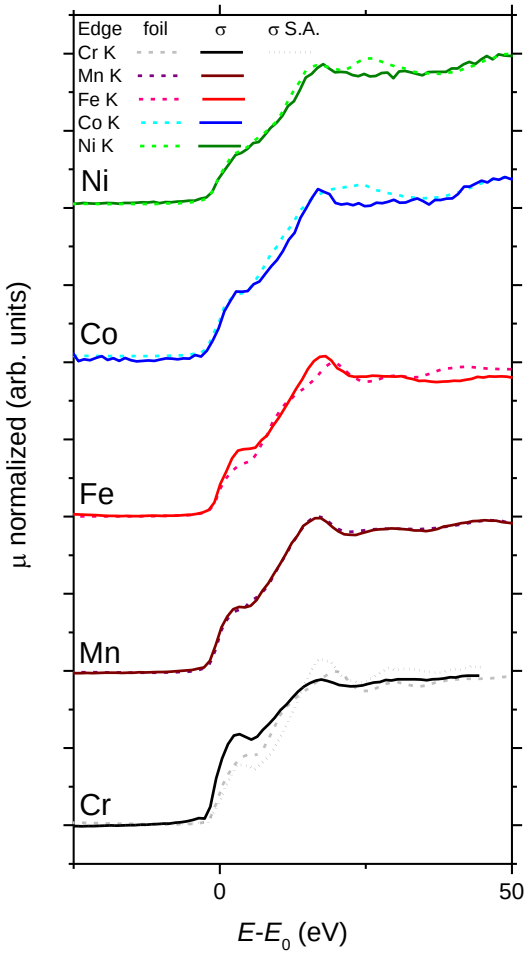

Fig. 3. XANES region for each K-edge spectrum of the quinary σ phase, superimposed with the corresponding reference foils and plotted as a function of E-E_0 (SOLEIL measurement, with E_0 the energy at the inflection point of the corresponding foil). In the case of Cr K-edge in σ, due to the high self-absorption (S.A.), a correction was applied.

EXAFS spectra were acquired at LISA-BM08 (ESRF experiment, Table S3), in addition to a second dataset of high-quality XANES spectra with a wider energy range than in SOLEIL. Data at LISA-BM08 was collected in transmission mode (i.e. with negligible self-absorption), so that XANES regions can be better compared with each other and with the reference foils. The XANES region of the reference foils and the quinary σ phase is depicted in Fig. S3 for comparison, similarly as SOLEIL data presented in Fig. 3. The XANES region of K-edge refers to bound states corresponding mainly to the s-p transition. The first spectra oscillations above the Fermi energy depend on the chemical environment and local symmetries around the absorbing element (generally up to 50 eV above the

edge). One can notice the differences in the reference foil spectral shape due the different crystal structures: *bcc* (Cr, Fe), α-Mn (Mn), *hcp* (Co) and *fcc* (Ni). However, as no differences are observed in XANES spectral shapes at any edge in the σ-phase (cf. Fig. S3 and Fig. 3), one can infer that the local symmetry around the absorbing elements of the σ phase is the same, i.e., the same local crystal structure is preserved independently of the edge measured. Note also how the XANES spectra of α-Mn, a topologically close-packed phase close to the σ phase with nearly the same type of coordination polyhedra, are comparable to the corresponding spectra of Mn in the σ phase. In Fig. 4 instead, the EXAFS data plotted in *R*-space show a remarkable difference in both bond distances and intensity depending on which absorber is considered. Nearest neighbor distances are on average shorter for Ni, Co, and Fe, on average longer for Cr, while Mn presents two clear shells, somewhat in between the two groups of Fe/Co/Ni, and Cr. These results already point to what will be shown by diffraction, i.e., that sites with higher CN are preferred by Cr – i.e., longer bond distances to accommodate more first nearest neighbors –, while Fe Co and Ni sit preferably in sites with lower CN – i.e., shorter bond distances. Mn falls in between, sitting on both lower and higher CN sites. Larger bond distances or CN for Cr and Mn against shorter distances for Fe, Co and Ni can also be correlated to the metallic radii of the elements, which decrease with the atomic number *Z*. Finally, from Fig. 4 one can notice that the signal drops substantially after the 1st shell, indicating the presence of high disorder beyond 3 Å, rationalized by the large atomic mixing, which induces an overlap of several bond distances with increasing distance from the absorber.

From the EXAFS spectra and KKR, dispersion coefficients *f'* and *f''* could be obtained. A comparison between tabulated and measured values as a function of energy is made in Fig. S4. The numerical values at the specific energies studied in the present work (7 eV below the edges) and used for the two structural refinements are shown in Table S4.

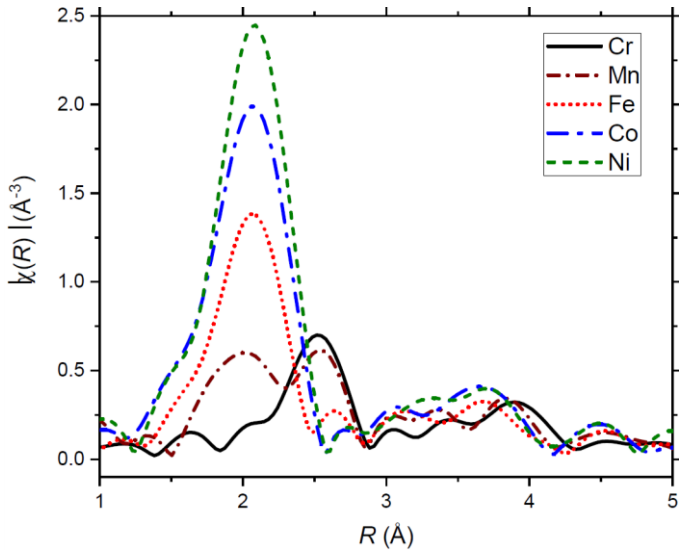

Fig. 4. Fourier transformed χ(k) EXAFS data into *R* space, |χ(*R*)|, of Cr, Mn, Fe, Co and Ni in the quinary σ phase obtained from EXAFS data. Fourier transformations were performed in the same *k*-range for each edge for clearer comparison, and no phase corrections were applied.

5.4. Resonant diffraction experiment

5.4.1. Measurement and refinement

Table S5 gives a list of the measured samples together with the dilution ratio and capillary diameter. A representative resonant XRD pattern for the Ni edge is shown with black data points in Fig. 5 while the other patterns are provided in Figs. S5-S10. Compared to the XRD for the Ni edge (Fig. 5), lower diffracted intensities were obtained at low energy (e.g., at the Cr edge, see Fig. S6). This is due to the smaller flux, the lower sensitivity of the detector at these energies, and the relevant air absorption (ca. 90% at 5982 eV). The Rietveld refinement of the XRD data is represented by red lines in Fig. 5 and Figs. S5-S10. The odd super-Lorentzian peak shape (see inset of Fig. 5) was modelled by introducing two states (cold-worked and undeformed) as mentioned above, resulting in a satisfactory description of the measured diffraction patterns. Each pattern was described first independently, then a joint refinement including the five patterns measured at the five edges of the constituting elements was carried out.

In addition to the two secondary phases originally present in the σ sample from the synthesis (*fcc* and spinel, less than 1 wt.% each), some unexpected presence of MnNi phase with the β-Mn crystal structure was observed. This corresponds to the second standard sample that had been prepared for *f'* calibration which was accidentally mixed with the σ phase during the preparation of the capillaries. Such MnNi phase contamination was identified, indexed and considered in the refinement. However, since its weight fraction is less than 5% and as the peaks are clearly separated from those of the σ phase, its presence does not affect the analysis and conclusions on site occupancies.

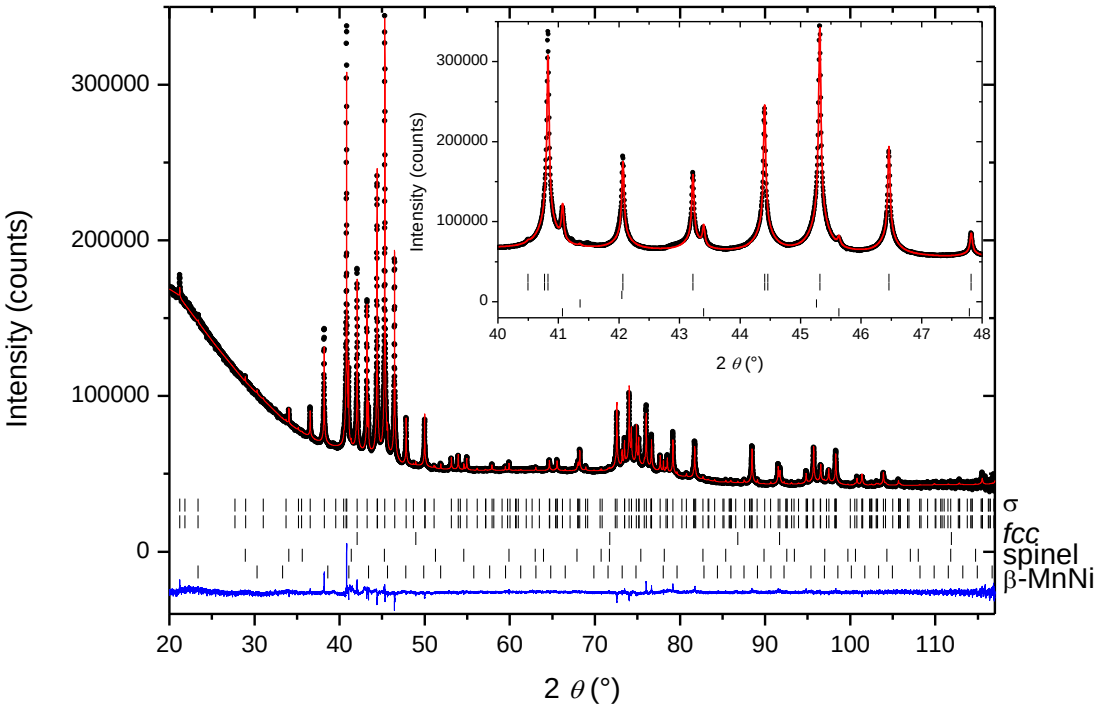

Fig. 5. Rietveld analysis of the XRD pattern of the quinary σ sample at 8325 eV (7 eV below the Ni edge). Experimental (points), calculated (red line) and difference (blue line below) patterns are shown. The markers from top to bottom show the positions of the σ phase (duplicated), *fcc*, spinel and β-MnNi.

5.4.2. Results for the reference sample

The β-MnCo reference sample was measured at both the Mn and Co edges. As it is not possible to refine *f'* in Fullprof, Mn/Co site occupancies were refined for different selected values of *f'*. Fig. 6 shows the refined site occupancy for Mn on site 8*c* at both edges. The obtained values are compared with the neutron diffraction refined value used as the reference and the *f'* value matching the neutron value can be determined. As shown in the figure, 'measured' and tabulated (Sasaki's) values for *f'* are in excellent agreement in both cases (-7.05 against -6.77 e^- at the Mn edge, -6.57 against -6.86 e^- at the Co edge). This shows that Sasaki's values can be used safely for all the edges.

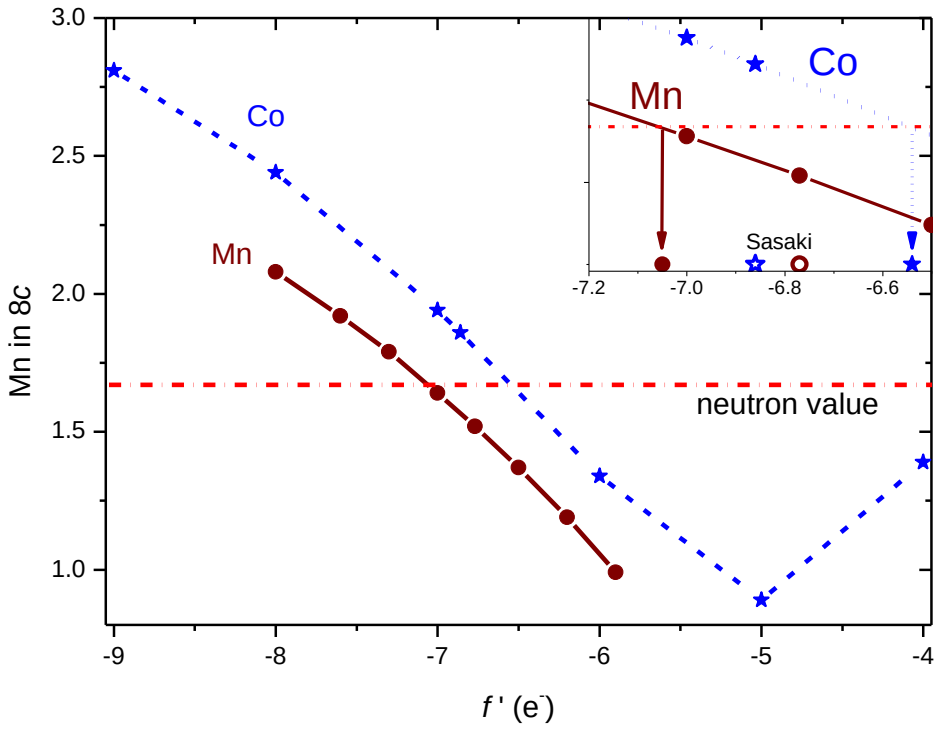

Fig. 6. Mn occupancy on site 8*c* of the β-Mn structure of $Mn_{60}Co_{40}$ refined on the XRD patterns measured 7 eV before the Mn and Co edges for different *f'* values of Mn and Co. The reference neutron value is shown as a horizontal line and the deduction of the *f'* values matching this value are shown in the inset. Comparison is made with Sasaki's tabulated values (open symbols).

5.4.3. Results for the quinary σ phase

The lattice parameters of the σ phase were found to change depending on the X-ray energy. The obtained results are plotted in Fig. S11. They correlate with a combination of increased absorption and increased flux. Therefore, a local increase in temperature related to X-ray absorption could be responsible for the observed increase in lattice parameters. From the known thermal expansion of the Cr–Mn σ phase [44], the difference in lattice parameters between 18 keV and the Ni edge could be explained by a temperature rise of 17°C.

The atomic coordinates (Table 1) refined from the 18 keV pattern (Fig. S5) are in perfect agreement with the average values reported for different σ phases (see Fig. 11 in Ref. [1]). Finally, the site occupancies as obtained from the joint refinement (*f'* from Sasaki) are shown in Table 1 and Fig. 7a. The (slightly) negative values are intentionally left because they fall into uncertainty. This shows that no additional constraint has been set and that otherwise positive values are spontaneously obtained, as an indicator of the quality of the analysis. The refined site occupancies using the *f'* values from KKR are given in Fig. S12 and Table S6. The obtained values are quite comparable to those obtained using the *f'* values from Sasaki, i.e., all values are within three times the standard deviation, corresponding to the Bérar and Lelann's estimate [34] of the accuracy (see Section 3.5.).

From the experimentally determined site occupancies shown in Fig. 7a, Cr is found to preferentially partition to the sublattices with high CNs, namely 14 and 15 (4*f*, 8i_1, and 8*j*) while Co, Ni and Fe to a lower degree mainly occupy the sites with the lowest CN of 12 (2*a* and 8i_2). Except for site 2*a* where Mn is completely absent, it is the element that is the most evenly distributed among the different sites, although it still shows a slight preference for sites with high CNs, in line with qualitative EXAFS results presented in Fig. 4

Table 1: Complete structural description including site occupancies (estimated standard deviation: 0.1 atom) obtained for the quinary σ phase ($P4_2/mnm$) from the joint refinement of the five resonant diffraction data. Lattice parameters refined from the 18 keV pattern are a = 8.7995(1) Å and c = 4.5507(1) Å

	atomic coordinates			occupancies in atoms				
site (CN)	*x*	*y*	*z*	Cr	Mn	Fe	Co	Ni
2*a* (12)	0	0	0	0.23	-0.01	0.48	0.88	0.42
4*f* (15)	0.3992(4)	0.3992(4)	0	2.65	1.05	0.31	0.05	-0.06
8i_1 (14)	0.4646(4)	0.1307(4)	0	4.34	1.67	0.97	0.44	0.57
8i_2 (12)	0.7403(4)	0.0662(4)	0	1.13	0.81	2.03	3.34	0.69
8*j* (14)	0.1823(2)	0.1823(2)	0.2505(12)	5.45	1.04	1.09	0.39	0.03

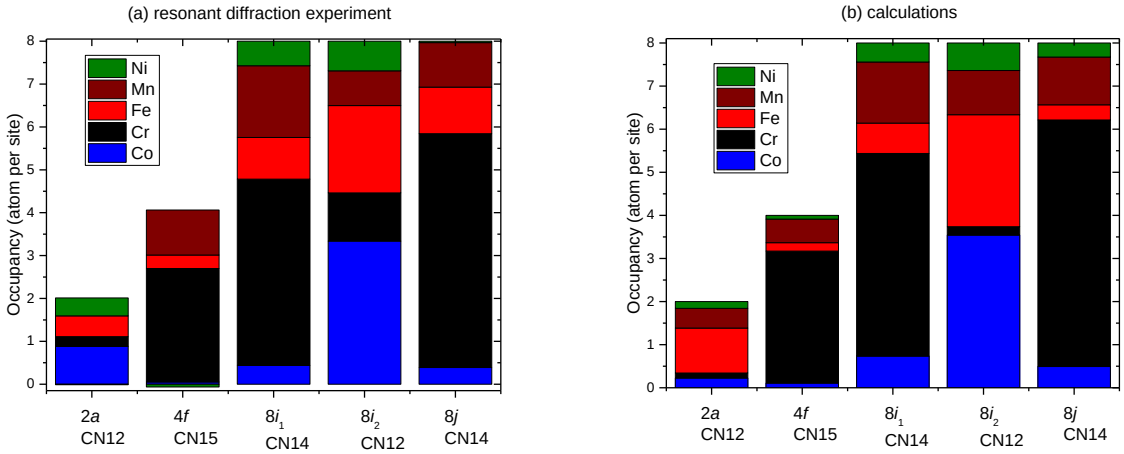

Fig. 7. Site occupancies of Cr, Mn, Fe, Co, and Ni on the five different sublattices of the quinary σ phase obtained experimentally from resonant diffraction experiment (*f'* values from Sasaki) (a), and by calculation at 1000 K with a thermodynamic model using the calculation of the 3125 enthalpies of formation of the possible ordered configuration and the Bragg-Williams approximation (b).

5.5. Calculation of site occupancies from DFT and machine learning

The energy of each configuration obtained by the machine learning approach based on the DFT results is given as spreadsheet file in the Supplementary Materials. The analysis of the ground state ('stable' configurations) shows that it is defined by 55 configurations (5 unary, 30 binary, 19 ternary and 1 quaternary). Among these, a statistical analysis shows that site 2*a* (CN12) is mostly occupied by Fe (34% of the configurations), site 4*f* (CN15) by Cr (60%), 8i_1 (CN14) by Cr (40%), 8i_2 by Co (35%) and 8*j* (CN14) by Cr (51%). This indicates a clear tendency of Cr to order on the sites with higher CNs, while Co and Fe prefer sites with lower CN, while Mn and possibly Ni are more evenly distributed (Mn and Ni have a slight tendency to partition on sites with high and low CNs, respectively). This is confirmed by the complete calculation of site occupancies for the composition studied in the present work (Fig. 7b).

6. Discussion

6.1. Refined f' values

Comparisons can be made between the different sets of *f'* value obtained from Sasaki, KKR and refined from the reference sample (Table S4). A very good agreement was obtained. This was expected given the very small difference between intermetallic compounds and pure metallic elements in terms of valence and electronic properties. This is also in line with a very recent report showing that the difference between Sasaki and measured *f'* is indeed minimal, at least below the edge, at the chosen energy value provided that one considers the relative energy difference from the edge and not

the absolute energy (not relevant in the present case since the edge position is found close to the free atom position) [45].

6.2. Analysis of site occupancies

The first observation is that the occupancies on the five different sites differ strongly from one site to the other. In this sense, the quinary σ phase is obviously ordered. However, the disorder or, better said, the extent of atom mixing is extremely large. This is already known for many σ phases in different binary systems, although the degree of disorder depends strongly on the system (e.g., the σ phase in the Ta–Al system is very ordered while it is close to complete disorder in systems such as V–Re, Cr–Os and Cr–Ru [1]).

In the present quinary system, the following is observed in Fig. 7. Co has a strong tendency for the sites of CN12, which is also the case for Fe and Ni but in a less pronounced manner. On the other hand, Cr and Mn have a strong preference for the higher CN sites CN14 and 15. As detailed in Ref. [1], this can be explained by both geometric (larger atoms prefer higher CN) and electronic (atoms with less valence electrons prefer high CN) features. As in many other systems, no significant difference is observed between the two sites with CN14 ($8i_1$ and $8j$) and that with CN15 ($4f$). Similarly, the occupancies of the two sublattices with CN12 ($2a$ and $8i_2$) do not significantly differ. This shows that even in strongly multicomponent alloys, the Calphad two-sublattice model (first sublattice comprising $2a$ and $8i_2$; second sublattice: $4f$, $8i_1$ and $8j$) proposed for the σ phase [1] constitutes an excellent approximation and that there is no reason, as far as site occupancies are concerned, to use the more complex three-sublattice model in which sites with CN14 and 15 are separately accounted for . This last model is the one used in commercial databases such as TCNI and TCHEA. The calculation of site occupancies with one of these databases shown in Fig. S13 demonstrates that the Cr occupancy on site $4f$ is largely overestimated and that a two-sublattice model would have given better results. Otherwise, it is worth noting the very good agreement of site occupancies on the other sites.

Another comparison can be made with the σ phase present in binary systems. The latter phase exists in three of the ten possible binary systems obtained by a combination of the 5 elements: Cr–Mn, Cr–Fe and Cr–Co. In these three systems, site occupancies were reported in the literature [44, 46, 47] (see Figs. S14). The same site occupancy tendencies can be observed. This is confirmed by a simple calculation consisting in extrapolating the binary results into the quinary with the following assumptions: the distribution of Mn, Fe and Co is calculated from the binary systems in proportion to the composition in the quinary system, Ni for which no information is available is statistically distributed, Cr complements up to full occupancy of each site. The result is shown in Fig. S15 and presents a good agreement with the site occupancies obtained from the resonant diffraction experiment.

In this study, with 5 elements, the level of disorder is extremely large and originates from the significant disorder already present in the binary systems in relation to the close electronic and

geometric properties. The configurational entropy calculated for the determined configuration (S = 1.18 R, where R is the ideal gas constant) is significant compared to that of a fully ordered intermetallic phase (S = 0) and it represents a significant fraction of the configurational entropy of a fully disordered alloy with the same composition (S = 1.40 R) making the present sample a kind of 'high-entropy intermetallic compound'. It is already known that entropy is responsible for the stabilization of the σ phase in binary systems such as Mo–Re in which it exists only at high temperature. This is also true for multi-component systems, where the entropy is much larger. Another interesting point is that this feature challenges the concept of HEA according to which disordered solid solutions would be preferred in multicomponent alloys because their entropy is supposed to be larger than that of (perfectly ordered) intermetallic compounds. This concept breaks down when intermetallic compounds are also able to accommodate disorder, such as in the σ phase.

6.3. Comparison with calculated data

One can note the very good agreement between the experimental and calculated site occupancies in Figs. 7a and b showing that observed site occupancies are a direct expression of the relative thermodynamic stability of the different ordered compounds (Eq. 2). Not only a qualitative agreement is obtained regarding the site preference, but also a quantitative agreement with an average difference between the occupancies of 0.3 atom/site (i.e., 3 times the standard deviation, again corresponding to the Bérar and Lelann's estimate of the accuracy [34] (see Section 3.5.)) and a maximum of 0.9 atom/site for Cr in 8i_2. A similar agreement was already obtained in the authors' previous studies of binary [42, 48] and ternary [2, 49] σ phases, but it is the first time that a quinary phase is calculated (and measured).

6.4. EXAFS/XANES and comparison with resonant XRD

As mentioned in the introduction, EXAFS enables the calculation of anomalous scattering coefficients *f'* through the KKR and it also allows to accurately determine the bond lengths around each element, from which qualitative and quantitative information on site occupancy and atomic positions in the crystal structure could be derived.

For a first round of fit and comparison, for every Wyckoff site in the σ phase, the amplitude factor was fixed to the relative occupancy of each site according to diffraction and DFT results. Relative contributions of less than 3% were omitted, e.g., Cr, Mn in 2*a* site, Co, Ni in 4*f* site, and Ni in 8*j* site since it did not improve the fit outcome and just increased the number of free parameters. Both diffraction and DFT-based EXAFS fitting gave optimal residuals and comparable bond length results. Occupancy values obtained using the *f'* values from KKR were also tested with similar outcome as diffraction and DFT-based model. Fits were also performed with a disordered model, i.e., without preferred occupancy (still omitting relative contributions below 3%) but overall the ordered (e.g., diffraction) models gave much better residuals. Final fits were conducted according to the relative occupancy model proposed by diffraction and tabulated *f'* values. One EXAFS fitting example at the Cr

edge is depicted in R-space in Fig. 8, while fits conducted at every other K edge are shown in Supplementary Material (Figs. S16).

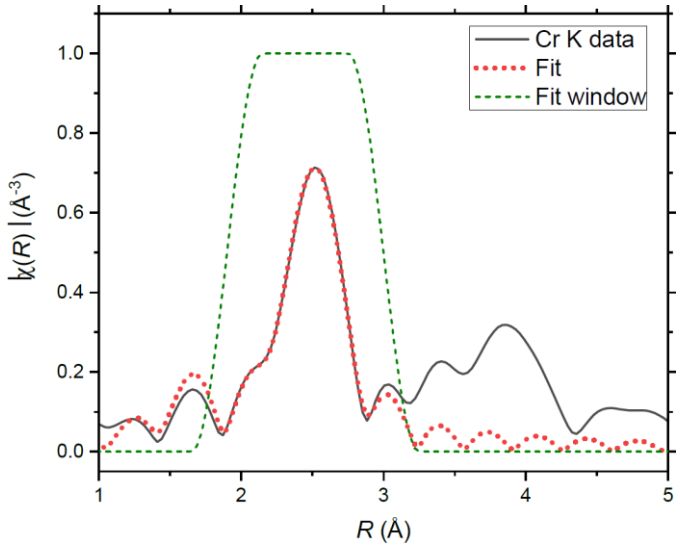

Fig. 8. First shell EXAFS refinements for Cr using the relative occupancies reported in Table 1. Data (black) and fit (red) in the corresponding window (green) are shown. Fitting in *R* space is used, and plots are not phase corrected.

A good agreement between the model and the spectra was achieved. A table summarizing the main refinement results is reported in Table S7. For the sake of clarity, bond lengths results are shown in Fig. 9 and compared with those obtained by diffraction. Here, it is worth noting that the EXAFS data are element specific while the diffraction data are not. Considering that a bond length from diffraction is an average bond length within the probed specimen volume, observed from a specific Wyckoff site (or atomic coordinates), and that an EXAFS refined bond length is an average bond length within the probed specimen volume measured for a specific element, a comparison can be carried out assuming that EXAFS bond lengths for a specific Wyckoff site should be roughly in line with the corresponding diffraction bond length, and that differences, if any, correlate with local distortions around that specific element. Higher uncertainties such as for Fe in 4*f* and Co in 8*j* are related to the small relative occupancies of these elements in the specific Wyckoff sites. Overall, a satisfactory agreement between the two methods is achieved, where refined EXAFS distances scatter close to the diffraction refined distances, see for example the 2*a* site where Fe-*M*, Co-*M*, Ni-*M* bond lengths are respectively slightly above, slightly below and within the uncertainty with the corresponding three refined bond lengths from diffraction. The Co-*M* bond lengths are in most cases the shortest bond lengths refined (in 2*a*, in 8i_1 with Cr-*M* and Mn-*M*, in 8i_2 with Fe-*M*), supporting what has been found earlier for *fcc* alloys [27, 50] and rationalized by both a short metallic radius and its low mixing enthalpy which does not make Co different from the other elements in the alloy. Cr-*M* bond lengths on the other hand tend to be larger in 4*f*, in 8i_2 and in 8*j*, explainable by the larger atomic radius of Cr compared to the other

alloying elements. Small local distortions, i.e., differences between Abs-*M* bond lengths and diffraction bond lengths are present for each Wyckoff site, close but different for every different alloying element.

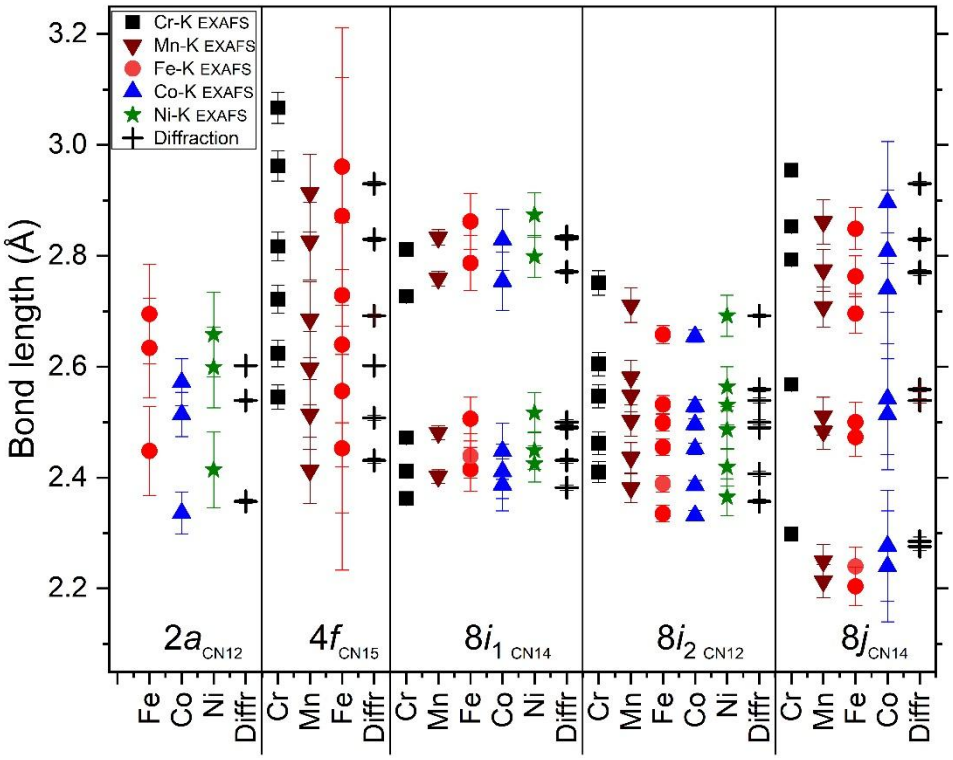

Fig. 9. Bond lengths obtained from EXAFS refinement at each K-edge (full markers) divided for each Wyckoff site (written at the bottom together with the CN), compared with bond lengths obtained by diffraction (black plus markers).

7. Conclusions

Site occupancies in the complex five-component Co–Cr–Fe–Mn–Ni σ phase have been studied using three different techniques: resonant diffraction, EXAFS and DFT calculations. Overall, the three techniques agree very well and confirm that the site occupancies are in line with the binary ones. For the resonant diffraction experiment, the dispersion coefficient *f'* has been obtained using three different approaches (diffraction, tabulated values, and KKR), which are also in good agreement with each other. The three techniques show that Co, followed by Fe and Ni to a lesser extent preferentially occupy the sites with a CN of 12 while Cr and Mn have a strong preference for the CN14 and CN15 sites. Similar site occupancies were found between the high CN sites $8i_1$, 8*j* and 4*f* (maximum deviation: 14 %). The occupancies of the two sublattices 2*a* and $8i_2$ (CN12) were also found to be similar (maximum deviation: 12 %). These results indicate that the Calphad two-sublattice

model proposed for the σ phase constitutes an excellent approximation that can be applied to multicomponent alloys.

The large disorder accommodated by the σ phase results in a strong entropic stabilization. For instance, the configurational entropy determined for the σ phase (S = 1.18 R, where R is the ideal gas constant) is much larger than that of a fully ordered intermetallic phase (S = 0) and it represents a significant fraction of S of a fully disordered alloy with the same composition (S = 1.40 R). The entropic stabilization is one of the reasons why the σ phase is commonly observed in many multicomponent systems, such as Co and Ni-base superalloys as well as steels (austenitic, ferritic, and duplex).

In future studies, the data on site occupancies that were determined in the present work will be used to accurately calculate some fundamental physical properties of the σ phase such as its elastic constants and the surface energies of the quasi close-packed planes, both of which related to the fracture toughness of this brittle intermetallic compound.

Acknowledgments:

G.L., Y.K. and R.Z. acknowledge funding through the collaborative research center SFB/TR 103, funded by the Deutsche Forschungsgemeinschaft DFG (Projects B8 and B5). A.F. acknowledges the financial support by the Deutsche Forschungsgemeinschaft, project FA1817/1-2. We thank F. d'Acapito (CNR-IOM) and A. Mirone (ESRF) for *f'* extraction by Kramers-Kronig relations from experimental EXAFS data acquired at LISA beamline (CRG-ESRF). The authors also acknowledge the center for interface-dominated high performance materials (ZGH) at the Ruhr University Bochum, Germany for the use of their electron microscope (JEOL JSM-7200F SEM). Calculations were performed using HPC resources at GENCI (No. A0060906175) and the supercomputer at IMR, Tohoku University (No. 16S0403). In addition, J.-C.C. thanks R. Xie and S. Junier for their practical help in extracting stable configurations.

References

[1] J.-M. Joubert, Crystal chemistry and Calphad modelling of the σ phase, Prog. Mater. Sci. 53 (2008) 528-583.
[2] K. Yaqoob, J.-C. Crivello, J.-M. Joubert, Comparison of the site occupancies determined by combined Rietveld refinement and by DFT calculations: the example of the ternary Mo-Ni-Re σ phase, Inorg. Chem. 51(5) (2012) 3071-3078.
[3] J. Barcik, The kinetics of σ-phase precipitation in AISI310 and AISI316 steels, Metall. Trans. A 14 (1983) 635-641.
[4] C.M. Rae, R.C. Reed, The precipitation of topologically close-packed phases in rhenium-containing superalloys, Acta Mater. 49 (2001) 4113-4125.
[5] K. Guruvidyathri, K.C. Hari Kumar, J.W. Yeh, B.S. Murty, Topologically close-packed phase formation in high entropy alloys: a review of Calphad and experimental results, JOM 69(11) (2017) 2113-2124.

[6] G. Laplanche, S. Berglund, C. Reinhart, A. Kostka, F. Fox, E.P. George, Phase stability and kinetics of σ-phase precipitation in CrMnFeCoNi high-entropy alloys, Acta Mater. 161 (2018) 338-351.
[7] E.O. Hall, S.H. Algie, The sigma phase, Metall. Rev. 11 (1966) 61-88.
[8] K. Kishida, M. Okutani, H. Inui, Direct observation of zonal dislocation in complex materials by atomic-resolution scanning transmission electron microscopy, Acta Mater. 228 (2022) 117756.
[9] D.Y. Kobayashi, S. Wolinec, Evaluation of the low corrosion resistant phase formed during the sigma phase precipitation in duplex stainless steels, Materials Research 2(4) (1999) 239-247.
[10] J. Zhang, G.M. Muralikrishna, A. Asabre, Y. Kalchev, J. Müller, B. Butz, S. Hilke, H. Rösner, G. Laplanche, S.V. Divinski, G. Wilde, Tracer diffusion in the σ phase of the CoCrFeMnNi system, Acta Mater. 203 (2021) 116498.
[11] G. Laplanche, Growth kinetics of σ-phase precipitates and underlying diffusion processes in CrMnFeCoNi high-entropy alloys, Acta Mater. 199 (2020) 193-208.
[12] K. Kishida, M. Okutani, H. Suzuki, H. Inui, M. Heilmaier, D. Raabe, Room-temperature deformation of single crystals of the sigma-phase compound FeCr with the tetragonal $D8_b$ structure investigated by micropillar compression, Acta Mater. 249 (2023) 118829.
[13] B. Cantor, I.T.H. Chang, P. Knight, A.J.B. Vincent, Microstructural development in equiatomic multicomponent alloys, Mater. Sci. Eng. A 375-377 (2004) 213-218.
[14] S.G. Fries, B. Sundman, Using Re-W sigma phase first-principles results in the Bragg-Williams approximation, Phys. Rev., B 66 (2002) 012203.
[15] J.-C. Crivello, J.-M. Joubert, N. Sokolovska, Supervised deep learning prediction of the formation enthalpy of complex phases using a DFT database: the σ phase as an example, Comput. Mater. Sci. 201 (2022) 110864.
[16] J.-L. Hodeau, V. Favre-Nicolin, S. Bos, H. Renevier, E. Lorenzo, J.-F. Berar, Resonant diffraction, Chem. Rev. 101 (2001) 1843-1867.
[17] H. Palancher, J.-L. Hodeau, C. Pichon, J.-F. Bérar, J.F. Lynch, B. Rebours, J. Rodríguez-Carvajal, Direct localization of atoms in mixed-occupancy powders by resonant contrast diffraction, Angew. Chem. Int. Ed. 44 (2005) 1725-1729.
[18] H. Palancher, S. Bos, J.-F. Bérar, I. Margiolaki, J.-L. Hodeau, X-ray resonant powder diffraction, European Physical Journal Special Topics 208 (2012) 275-289.
[19] S. Welzmiller, P. Urban, F. Fahrnbauer, L. Erra, O. Oeckler, Determination of the distribution of elements with similar electron counts: a practical guide for resonant X-ray scattering, J. Appl. Crystallogr. 46 (2013) 769-778.
[20] S. Sasaki, Numerical tables of anomalous scattering factors calculated by the Cromer and Liberman's method, National Laboratory for High Energy Physics, Tsukuba, Japan, 1989, pp. 1-139.
[21] D.T. Cromer, D.A. Liberman, Relativistic calculation of anomalous scattering factors for X rays, J. Chem. Phys. 53 (1970) 1891-1898.
[22] D.T. Cromer, D.A. Liberman, Anomalous dispersion calculations near to and on the long-wavelength side of an absorption edge, Acta Crystallogr. A37 (1981) 267-268.
[23] G. Evans, R.F. Pettifer, CHOOCH: a program for deriving anomalous-scattering factors from X-ray fluorescence spectra, J. Appl. Crystallogr. 34 (2001) 82-86.
[24] J.-M. Joubert, J.-C. Crivello, Crystallographic study of β-Mn solid solutions, to be published.
[25] B. Ravel, M. Newville, ATHENA and ARTEMIS: interactive graphical data analysis using IFEFFIT, Physica Scripta T115 (2005) 1007-1010.
[26] P. Dreier, P. Rabe, W. Malzfeldt, W. Niemann, Anomalous X-ray scattering factors calculated from experimental absorption spectra, J. Phys. C: Solid State Phys. 17(17) (1984) 3123-3136.
[27] A. Fantin, G. Orazio Lepore, A.M. Manzoni, S. Kasatikov, T. Scherb, T. Huthwelker, F. d'Acapito, G. Schumacher, Short-range chemical order and local lattice distortion in a compositionally complex alloy, Acta Mater. 193 (2020) 329-337.
[28] J. Rodríguez-Carvajal, Fullprof: a program for Rietveld refinement and pattern matching analysis, XV Congress of Int. Union of Crystallography, Satellite Meeting on Powder Diffraction (1990) 127.
[29] J. Rodríguez-Carvajal, Recent developments of the program FULLPROF, Commission on Powder Diffraction, Newsletter (26) (2001) 12-19.
[30] J.-M. Joubert, R. Cerný, M. Latroche, A. Percheron-Guégan, K. Yvon, Site occupancies in $LaNi_5$ three-substituted compound determined by means of multiwavelength X-ray powder diffraction, J. Appl. Crystallogr. 31 (1998) 327-332.
[31] J.-M. Joubert, Crystal structure, hydrogen absorption properties and crystal structure of the deuterides of some Nb-Ni derived μ phase compounds, J. Solid State Chem. 178 (2005) 1620-1629.
[32] J.-M. Joubert, R. Cerný, H. Emerich, Mixed site occupancies in μ-Zr-Nb-Al by resonant powder diffraction, Z. Kristallogr. Suppl. 26 (2007) 311-316.

[33] T. Bartoli, J.-M. Joubert, K. Provost, E. Elkaim, V. Paul-Boncour, J. Monnier, J. Moscovici, L. Bessais, Site occupancy determination in Th_2Zn_{17}- and $TbCu_7$-types $Sm_2Fe_{17-x}Co_x$ compounds using synchrotron resonant diffraction, Inorg. Chem. 60 (2021) 1533-1541.
[34] J.-F. Bérar, P. Lelann, E.S.D.'s and estimated probable error obtained in Rietveld refinements with local correlations, J. Appl. Crystallogr. 24 (1991) 1-5.
[35] B. Sundman, J. Ågren, A regular solution model for phases with several components and sublattices, suitable for computer applications, J. Phys. Chem. Solids 42 (1981) 297-301.
[36] J.-C. Crivello, R. Souques, N. Bourgeois, A. Breidi, J.-M. Joubert, ZenGen: a tool to generate ordered configurations for systematic DFT calculations: example of the Cr-Mo-Ni-Re system, Calphad: Comput. Coupling Phase Diagrams Thermochem. 51 (2015) 233-240.
[37] P.E. Blöchl, Projector augmented-wave method, Phys. Rev., B 50(24) (1994) 17953-17979.
[38] G. Kresse, D. Joubert, From ultrasoft pseudopotentials to the projector augmented-wave method, Phys. Rev., B 59(3) (1999) 1758-1775.
[39] J.P. Perdew, K. Burke, M. Ernzerhof, Generalized gradient approximation made simple, Phys. Rev. Lett. 77(18) (1996) 3865-3868.
[40] J.P. Perdew, K. Burke, M. Ernzerhof, ERRATA: Generalized gradient approximation made simple [Phys. Rev. Lett. 77, 3865 (1996)], Phys. Rev. Lett. 78(7) (1997) 1396.
[41] H.J. Monkhorst, J.D. Pack, Special points for Brillouin-zone integrations, Phys. Rev., B 13 (1976) 5188-5192.
[42] A. Breidi, M. Andasmas, J.-C. Crivello, N. Dupin, J.-M. Joubert, Experimental and computed phase diagrams of the Fe–Re system, J. Phys.: Condens. Matter 26 (2014) 485402.
[43] F. Pedregosa, G. Varoquaux, A. Gramfort, V. Michel, B. Thirion, O. Grisel, M. Blondel, P. Prettenhofer, R. Weiss, V. Dubourg, J. Vanderplas, A. Passos, D. Cournapeau, M. Brucher, M. Perrot, E. Duchesnay, Scikit-learn: machine learning in Python, Journal of Machine Learning Research 12 (2011) 2825-2830.
[44] J.-M. Joubert, Intermetallic compounds of the Cr-Mn system investigated using *in situ* powder neutron diffraction: the reported order-disorder transformation of the σ phase elucidated, Intermetallics 146 (2022) 107580.
[45] F. Meurer, O.V. Dolomanov, C. Hennig, N. Peyerimhoff, F. Kleemis, H. Puschmann, M. Bodensteiner, Refinement of anomalous dispersion correction parameters in single-crystal structure determinations, IUCrJ 9 (2022) 604-609.
[46] S.H. Algie, E.O. Hall, Site ordering in some σ phase structures, Acta Crystallogr. 20 (1966) 142.
[47] H.L. Yakel, Atom distribution in sigma phases. I. Fe and Cr atom distribution in a binary sigma phase equilibrated at 1063, 1013 and 923 K, Acta Crystallogr. B39 (1983) 20-28.
[48] J.-C. Crivello, J.-M. Joubert, First principles calculations of the σ and χ phases in the Mo-Re and W-Re systems, J. Phys.: Condens. Matter 22 (2010) 035402.
[49] J.-M. Joubert, M. Andasmas, J.-C. Crivello, Irregular homogeneity domains in ternary intermetallic systems, Appl. Sci. 5 (2015) 1570-1589.
[50] A. Fantin, C.T. Cakir, S. Kasatikov, G. Schumacher, A.M. Manzoni, Effects of heat treament on microstructure, hardness and local structure in a compositionally complex alloy, Materials Chemistry and Physics 276 (2022) 125432.